Enhanced Polysulfide Conversion with Highly Conductive and Electrocatalytic Iodine-Doped Bismuth Selenide Nanosheets in Lithium–Sulfur Batteries

Mengyao Li, Dawei Yang,* Jordi Jacas Biendicho, Xu Han, Chaoqi Zhang, Kun Liu, Jiefeng Diao, Junshan Li, Jing Wang, Marc Heggen, Rafal E. Dunin-Borkowski, Jiaao Wang,* Graeme Henkelman, Joan Ramon Morante, Jordi Arbiol, Shu-Lei Chou,* and Andreu Cabot*

The shuttling behavior and sluggish conversion kinetics of intermediate lithium polysulfides (LiPS) represent the main obstacles to the practical application of lithium–sulfur batteries (LSBs). Herein, an innovative sulfur host is proposed, based on an iodine-doped bismuth selenide (I-Bi$_2$Se$_3$), able to solve these limitations by immobilizing the LiPS and catalytically activating the redox conversion at the cathode. The synthesis of I-Bi$_2$Se$_3$ nanosheets is detailed here and their morphology, crystal structure, and composition are thoroughly. Density-functional theory and experimental tools are used to demonstrate that I-Bi$_2$Se$_3$ nanosheets are characterized by a proper composition and micro- and nano-structure to facilitate Li$^+$ diffusion and fast electron transportation, and to provide numerous surface sites with strong LiPS adsorbability and extraordinary catalytic activity. Overall, I-Bi$_2$Se$_3$/S electrodes exhibit outstanding initial capacities up to 1500 mAh g^{-1} at 0.1 C and cycling stability over 1000 cycles, with an average capacity decay rate of only 0.012% per cycle at 1 C. Besides, at a sulfur loading of 5.2 mg cm^{-2}, a high areal capacity of 5.70 mAh cm^{-2} at 0.1 C is obtained with an electrolyte/sulfur ratio of 12 μL mg^{-1}. This work demonstrated that doping is an effective way to optimize the metal selenide catalysts in LSBs.

1. Introduction

There is an urgent need for a new generation of rechargeable energy storage devices that offer a step higher capacity and durability, well beyond the limitations of current lithium-ion batteries (LIBs). Among the possible candidates, lithium–sulfur batteries (LSBs) attract significant attention due to their very high theoretical specific energy, 2600 Wh Kg^{-1}, their potential for low cost associated with the abundance of sulfur, and their lack of toxicity.[1–5] However, their practical use is still hindered by the electrically insulating nature of sulfur and its discharge products (Li$_2$S/Li$_2$S$_2$),[6–8] a low utilization of the active material, and a moderate cycling stability associated with the large volume expansion of the cathode upon lithiation[9–12] and the shuttle of the soluble intermediate lithium polysulfides (LiPS).[13–15] These

M. Y. Li, D. W. Yang, J. J. Biendicho, C. Q. Zhang, J. R. Morante, A. Cabot
Catalonia Institute for Energy Research – IREC
Sant Adrià de Besòs
Barcelona 08930, Spain
E-mail: ydawei@irec.cat; davidyangseu@gmail.com; acabot@irec.cat
M. Y. Li, D. W. Yang, C. Q. Zhang, J. R. Morante
Department of Electronic and Biomedical Engineering
Universitat de Barcelona
Barcelona 08028, Spain
X. Han, J. Arbiol
Catalan Institute of Nanoscience and Nanotechnology (ICN2)
CSIC and BIST
Campus UAB
Bellaterra, Barcelona, Catalonia 08193, Spain
K. Liu
Institute of Materials and Technology
Dalian Maritime University
Dalian 116026, China

J. F. Diao, J. A. Wang, G. Henkelman
Department of Chemistry and the Oden Institute for Computational
Engineering and Sciences
The University of Texas at Austin
Austin, TX 78712, USA
E-mail: wangjiaao0720@utexas.edu
J. Li
Institute of Advanced Study
Chengdu University
No. 2025, Chengluo Avenue, Chengdu
Sichuan Province 610106, China
J. Wang
State Grid Anhui Ultra High Voltage Company
No. 8, Jincui Road, Changfeng County
Hefei, Anhui Province 231100, China
M. Heggen, R. E. Dunin-Borkowski
Ernst Ruska-Centre for Microscopy and Spectroscopy with Electrons
and Peter Grünberg
Institute Forschungszentrum Jü lich GmbH
52425 Jülich, Germany
J. Arbiol, A. Cabot
ICREA, Pg
Lluís Companys 23, Barcelona, Catalonia 08010, Spain

ADVANCED
SCIENCE NEWS
www.advancedsciencenews.com

ADVANCED
FUNCTIONAL
MATERIALS
www.afm-journal.de

drawbacks call for an improved design and engineering of the sulfur cathode.[16–20]

Conductive porous carbons have been widely used to improve the electrical conductivity of the cathode, encapsulate sulfur, and restrain the dissolution and diffusion of LiPS.[21,22] However, the encapsulation of sulfur within porous carbon can be detrimental to the cathode redox reaction kinetics by reducing sulfur reactivity and slowing the desolvation process.[23,24] To overcome current cathode limitations, metal-based compounds and metal-organic frameworks have been added to strengthen the chemical interaction with LiPS and reduce the shuttle effect.[25–30] Among the tested metal compounds, sulfides such as MoS_2, VS_2, CoS_2, Ni_3S_2, and Sb_2S_3, have demonstrated particularly strong sulfiphilic ability toward LiPS trapping and low lithiation voltages.[31–36] However, cathodes based on metal sulfides are generally characterized by moderate electrical conductivities, limited sulfur utilization, insufficient cycling stability, and low rate capabilities.[37–41]

Recently, we and others have demonstrated metal selenides, such as ZnSe, $NbSe_2$, and $NiCo_2Se_4$, as promising sulfur hosts in LSB cathodes, owing to their notable polarity, excellent catalytic activity, and high electrical conductivity.[3,5,34,42,43] However, among the extended family of possible chalcogenides, a particularly interesting candidate has been so far overlooked. Bismuth selenide (Bi_2Se_3) is generally an n-type degenerated semiconductor, with a low bandgap of 0.3 eV, that is widely used in the field of thermoelectricity due to its high electrical conductivity.[41,42] Its n-type electronic behavior is related to the presence of Se vacancies that act as electron donors. Bi_2Se_3 has a layered crystal structure consisting of stacks of covalently bonded quintuple atomic layers, Se—Bi—Se—Bi—Se, that are held together by weak van der Waals interactions. Such high electrical conductivity and layered structure are highly suitable for its use as sulfur hosts in LSB cathodes. Besides, the variable chemical valences of Bi and Se anticipate a high potential catalytic activity.

In this work, we evaluate the potential of Bi_2Se_3 and iodine-doped Bi_2Se_3 nanosheets as sulfur hosts in LSBs. We first detail the synthesis of Bi_2Se_3 nanosheets using a high yield and scalable solution-based method. These Bi_2Se_3 nanosheets were doped with iodine to increase their electrical conductivity.[44] The obtained material is used as the sulfur host in LSB cathodes and its performance is experimentally analyzed and computationally rationalized. Results demonstrate the I-Bi_2Se_3 nanosheets are not only characterized by higher electrical conductivities, as expected, but also provide enhanced confinement of LiPS and an excellent electrocatalytic activity towards the redox reaction of sulfur and lithium sulfide.

2. Results and Discussions

Bi_2Se_3 nanosheets, assembled into flower-like structures (Figure S1a, Supporting Information), were produced at 180 °C

S.-L. Chou
Institute for Carbon Neutralization
College of Chemistry and Materials Engineering
Wenzhou University
Wenzhou, Zhejiang 325035, China
E-mail: chou@wzu.edu.cn

from a basic solution containing bismuth nitrate, sodium selenite, and polyvinylpyrrolidone (see details in the experimental section in the Supporting Information). X-ray diffraction (XRD) analysis showed the nanosheets to have high crystallinity and their crystal structure to match the rhombohedral Bi_2Se_3 phase (JCPDS No. 00-033-0214, Figure S1b). High resolution transmission electron microscopy (HRTEM) characterization confirmed the Bi_2Se_3 rhombohedral phase (space group = Pbnm) with a = 11.6230 Å, b = 11.8310 Å, and c = 4.0900 Å (Figure S1c, Supporting Information). Besides, electron energy loss spectroscopy (EELS) chemical composition maps demonstrated a uniform distribution of both elements, Bi and Se, through the nanosheet (Figure S1d, Supporting Information).

Iodine ions were incorporated to pre-synthesized Bi_2Se_3 by dispersing the Bi_2Se_3 nanosheets in an aqueous solution of potassium iodide under vigorous stirring at room temperature for 48 h. Iodine-doped Bi_2Se_3 (I-Bi_2Se_3) nanosheets preserved the flower-like morphology and the rhombohedral crystal structure of undoped Bi_2Se_3 (**Figure 1**a,b,d). Energy dispersive X-ray spectrometer (EDX) analysis quantified the iodine concentration at a 4 at%. Besides, EELS chemical composition maps displayed a homogeneous distribution of Bi, Se, and I within the I-Bi_2Se_3 nanosheets (Figure 1c).

X-ray photoelectron spectroscopy (XPS) was used to determine the surface composition of I-Bi_2Se_3 and the chemical environment of its elements (Figure 1e). As a reference, Figure S2, Supporting Information, displays the XPS spectra of undoped Bi_2Se_3. The high-resolution Bi 4f XPS spectrum of I-Bi_2Se_3 was fitted with two doublets. The lowest energy doublet was associated with Bi^{3+} within a Bi_2Se_3 chemical environment (Bi $4f_{7/2}$ binding energy at 157.5 eV). The highest energy doublet was associated with Bi^{3+} within a more electronegative environment, as it could be Bi_2O_3, $Bi_2(SeO_3)_3$, Bi_2SeO_2, or another oxidized form of Bi_2Se_3 (Bi $4f_{7/2}$ binding energy at 158.5 eV).[45,46] The presence of an oxide component was related to the transportation and handling of the particles in the air. The Bi 4f XPS spectrum of Bi_2Se_3 displayed the same two doublets, but the one corresponding to Bi within Bi_2Se_3 was slightly shifted to lower binding energies (Bi $4f_{7/2}$ at 157.3 eV). The high-resolution Se 3d XPS spectrum was also fitted with two doublets, which were associated with Se^{2-} within Bi_2Se_3 (Se $3d_{5/2}$ at 52.8 eV) and SeO_2, $Bi_2(SeO_3)_3$, Bi_2SeO_2 or another form of Se within a more electronegative environment (Se $3d_{5/2}$ at 53.7 eV), related to the partial oxidation of the material surface.[44,47] The Se 3d XPS spectrum of Bi_2Se_3 also displayed two doublets, with the one associated with Se within Bi_2Se_3 being slightly shifted to lower binding energies (Se $3d_{5/2}$ at 52.8 eV). This correlated blue-shift of the Bi 4f and Se 3d XPS spectra of I-Bi_2Se_3 with respect to Bi_2Se_3 is associated with an upward shift of the semiconductor Fermi level, in agreement with the electronic doping role played by I^- ions at Se^{2-} sites. Finally, the high resolution I 3d XPS spectrum was fitted with two peaks, at 618.5 eV (I $3d_{5/2}$) and 630 eV ($3d_{3/2}$), which were associated with an I^{-1} chemical state.[48,49]

The electrical conductivity of both Bi_2Se_3 and I-Bi_2Se_3 samples decreased with temperature, implying a degenerated semiconductor behavior (Figure 1f). Besides, the Seebeck coefficient of both samples was negative in the whole temperature range, implying an n-type conductivity. With the introduction
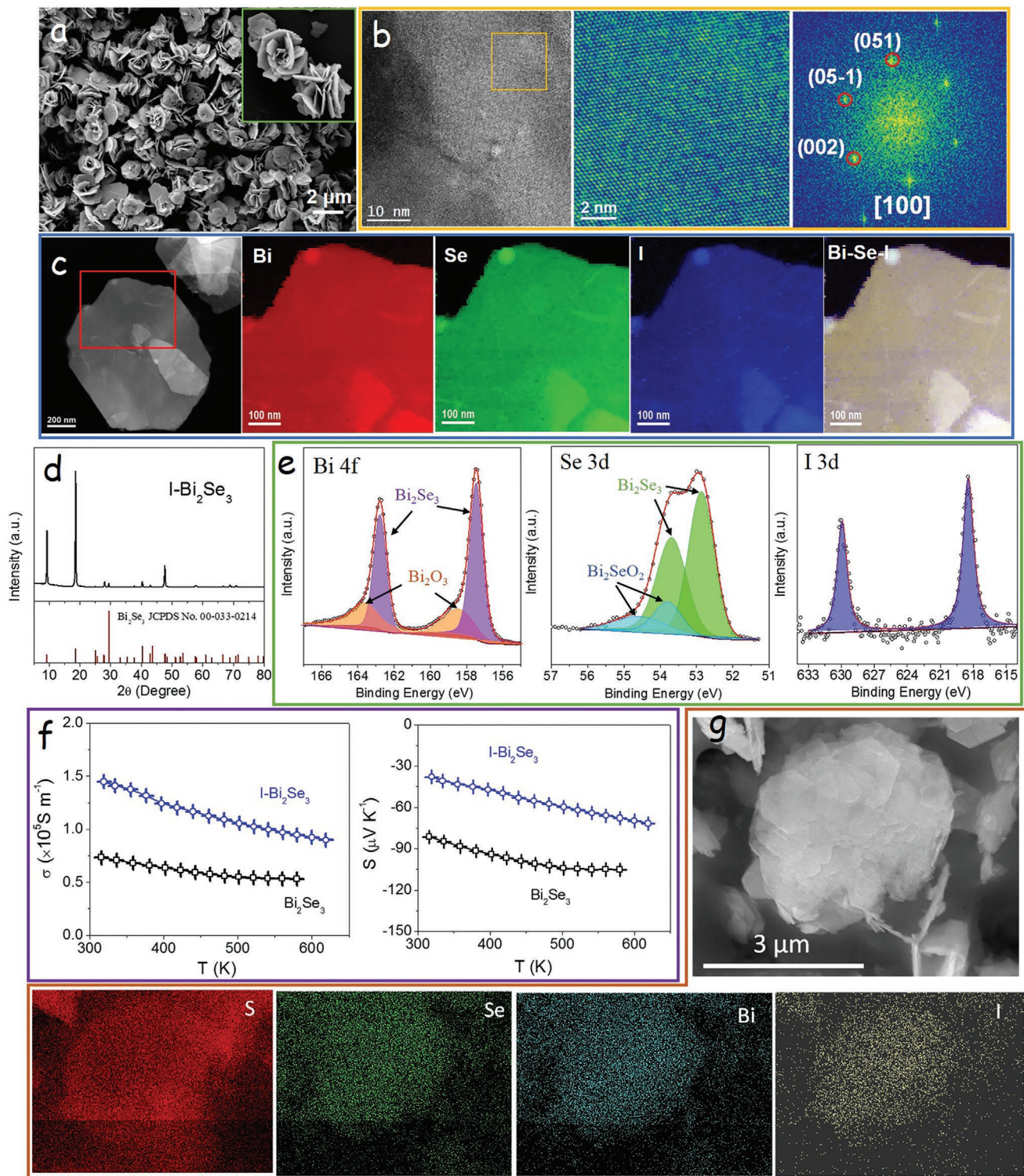
Figure 1. Characterization of I-Bi$_2$Se$_3$ nanosheets: a) SEM image. b) HRTEM image and its corresponding power spectrum. c) EELS chemical composition maps obtained from the red squared area of the STEM micrograph. Individual Bi N$_{6,7}$-edges at 157 eV (red), Se M$_1$-edge at 232 eV (green), I M$_{4,5}$-edge 619 eV (blue), and composite of Bi—Se—I. d) XRD pattern. e) Bi 4f, Se 3d, and I 3d high-resolution XPS spectra. f) Temperature dependence of the electrical conductivity (σ) and Seebeck coefficient (S) of Bi$_2$Se$_3$ and I-Bi$_2$Se$_3$. g) SEM image EDX elemental maps of I-Bi$_2$Se$_3$/S composite.

of iodine, a twofold increase of the Bi_2Se_3 electrical conductivity was measured. The rise of the electrical conductivity was correlated with a decrease of the absolute value of the Seebeck coefficient, which is consistent with an increase of the charge carrier concentration with the iodine doping.

Sulfur was introduced via a melt infiltration process (see details in the experimental section).[5,34] The morphology of the $I-Bi_2Se_3/S$ composite resembled that of the original $I-Bi_2Se_3$ nanosheets assembled into flowers (Figure 1g). The XRD pattern of $I-Bi_2Se_3/S$ confirmed the successful loading of crystalline sulfur within $I-Bi_2Se_3/S$ composite (Figure S3, Supporting Information). EDX elemental maps displayed a homogeneous distribution of the four elements, I, Bi, Se, and S, within the composite (Figure 1g), with no independent sulfur particle. Upon sulfur incorporation, the nitrogen adsorption-desorption isotherms showed the Brunauer–Emmett–Teller (BET) specific surface area to be reduced from 128.6 m^2 g^{-1} for $I-Bi_2Se_3$ to 13.2 m^2 g^{-1} for $I-Bi_2Se_3/S$ (Figure S5, Supporting Information). Besides, the pore volume of $I-Bi_2Se_3$, decreased from 0.5 cm^3 g^{-1}, to 0.026 cm^3 g^{-1} with the incorporation of sulfur, which further demonstrated the successful loading of sulfur within the pore structure of the assembled $I-Bi_2Se_3$ nanosheets. The loaded mass of sulfur was quantified at ≈70.2 wt% using thermogravimetry analysis (TGA, Figure S4, Supporting Information).

The interaction between $I-Bi_2Se_3$ and LiPS was analyzed using Li_2S_4 adsorption tests (see details in Experimental Section). **Figure 2**a,b displays an optical image and the UV–vis spectra of several flasks that contain 3 mL of a 0.01 M Li_2S_4 solution and the exact same amount (20 mg) of each of the tested adsorbers, Super P, Bi_2Se_3, or $I-Bi_2Se_3$, after overnight aging. We observe that the color of the Li_2S_4 solution, and the absorbance intensity in the 400–500 nm region associated with Li_2S_4, was almost unchanged in the presence of Super P. On the contrary, the color of the Li_2S_4 solutions and the visible absorbance became much lighter in the presence of Bi_2Se_3 and especially $I-Bi_2Se_3$, suggesting a strong chemical interaction of LiPS with Bi_2Se_3 and particularly with $I-Bi_2Se_3$. $I-Bi_2Se_3$ exhibited the clearest solution and the lowest visible absorption, indicating the presence of the lowest amount of Li_2S_4 in the solution and thus the greatest LiPS adsorbability.

Figure 2c displays the high-resolution Bi 4f XPS spectra of $I-Bi_2Se_3$ before and after the Li_2S_4 adsorption test. Compared with the original spectra of $I-Bi_2Se_3$, the Bi 4f binding energies in $I-Bi_2Se_3-Li_2S_4$ shifted to lower values, revealing the interaction of S with surface Bi.[5]

Density functional theory (DFT) calculations were carried out to further evaluate the interaction between LiPS and $I-Bi_2Se_3$. The optimized LiPS adsorption configuration at six different lithiation stages (Li_2S, Li_2S_2, Li_2S_4, Li_2S_6, Li_2S_8, and S_8) on the Bi_2Se_3 and $I-Bi_2Se_3$ surfaces are displayed in Figures S6 and S7, Supporting Information. DFT calculations showed the binding energies (E_b) of LiPS species at the six tested lithiation stages to be higher on $I-Bi_2Se_3$ than on Bi_2Se_3 (Figure 2e). Figure 2d displays the relaxed adsorption structure of Li_2S_4 on the (110) surface of Bi_2Se_3 and $I-Bi_2Se_3$, respectively. The calculated E_b for the relaxed configuration of Li_2S_4 absorbed on Bi_2Se_3 (110) and $I-Bi_2Se_3$ (110) surfaces are −1.27 and −2.09 eV, respectively. These DFT results demonstrate a strong interaction between

S within LiPS and Bi within Bi_2Se_3, which corroborates the sulfiphilic character of Bi_2Se_3. These results also demonstrate that the presence of I on the Bi_2Se_3 surface further increases the absolute value of the binding energy, thus favoring LiPS adsorption and hence potentially reducing the shuttle effect.

Figure 2f displays the band structure and density of states (DOS) of Bi_2Se_3 and $I-Bi_2Se_3$. Calculations show $I-Bi_2Se_3$ to be characterized by a significantly smaller bandgap than Bi_2Se_3. Besides, consistently with results from electrical transport measurements, DFT calculations show the presence of iodine to upward shift the Fermi level, which appears lying within the $I-Bi_2Se_3$ conduction band thus promoting the intrinsic conductivity and degenerated/metallic character of $I-Bi_2Se_3$.[50]

Figure 2g and Figure S8, Supporting Information exhibit the initial state, transition state, and final state of Li_2S decomposition on Bi_2Se_3 and $I-Bi_2Se_3$. The calculated energy barrier for Li_2S decomposition on Bi_2Se_3 and $I-Bi_2Se_3$ surfaces was 0.56 and 0.98 eV, respectively (Figure 2g). These results demonstrate that $I-Bi_2Se_3$ can greatly reduce the Li_2S decomposition energy barrier and enhance the redox reversibility between Li_2S and LiPS.

The S reduction pathways on both Bi_2Se_3/S and $I-Bi_2Se_3/S$ cathodes were calculated considering the overall reversible reaction between Li_2S and S_8 + Li. The first step of the discharge process involves the reduction of S_8 with two Li^+ to form Li_2S_8. Subsequently, Li_2S_8 undergoes further reduction to three intermediate LiPS, Li_2S_6, Li_2S_4, Li_2S_2, and finally Li_2S as the end product. Figure 2h displays the optimized configuration of the intermediates and their Gibbs free energy profiles. For both materials, Bi_2Se_3/S and $I-Bi_2Se_3/S$, the largest increase of Gibbs free energy was obtained for the conversion from Li_2S_2 to Li_2S, suggesting this step as the rate-limiting for the discharge process.[51] The free energy increase of this step was lower for $I-Bi_2Se_3$ (0.71 eV) than for Bi_2Se_3 (0.89 eV), suggesting that the reduction of S was more thermodynamically favorable on $I-Bi_2Se_3$ than on Bi_2Se_3.

The electrochemical performance of Li–S coin cells containing an $I-Bi_2Se_3/S$ cathode was evaluated and compared with that of cells based on Bi_2Se_3/S and Super P/S cathodes. **Figure 3**a displays the CV curves obtained at 0.1 mV s^{-1}. All cathodes displayed two well-defined cathodic peaks associated with the reduction of solid-state S into soluble long-chain LiPS (Li_2S_x, 4 < x < 8, peak C1) and the subsequent conversion of these LiPS to insoluble Li_2S_2/Li_2S (peak C2).[3] Besides, an anodic peak is observed (peak A), corresponding to the reverse oxidation conversion from Li_2S to LiPS and ultimately to S.[34] The peak current density of the reduction and oxidation peaks of $I-Bi_2Se_3/S$ was clearly higher than that of the two reference cathodes, all containing the same amount of sulfur, thus suggesting a higher sulfur utilization in the $I-Bi_2Se_3/S$ cathode. The C2 peak of the $I-Bi_2Se_3/S$ cathode at about 2.042 V shows a much larger current density and is slightly shifted to a higher potential compared with the other cathodes, suggesting a promoted conversion of LiPS to insoluble Li_2S_2/Li_2S within the $I-Bi_2Se_3/S$ cathode. Besides, the A oxidation peak of $I-Bi_2Se_3/S$ is shifted to a lower potential, 2.33 V, and displays a larger current density, indicating an enhanced Li_2S decomposition (Figure 3a,b).
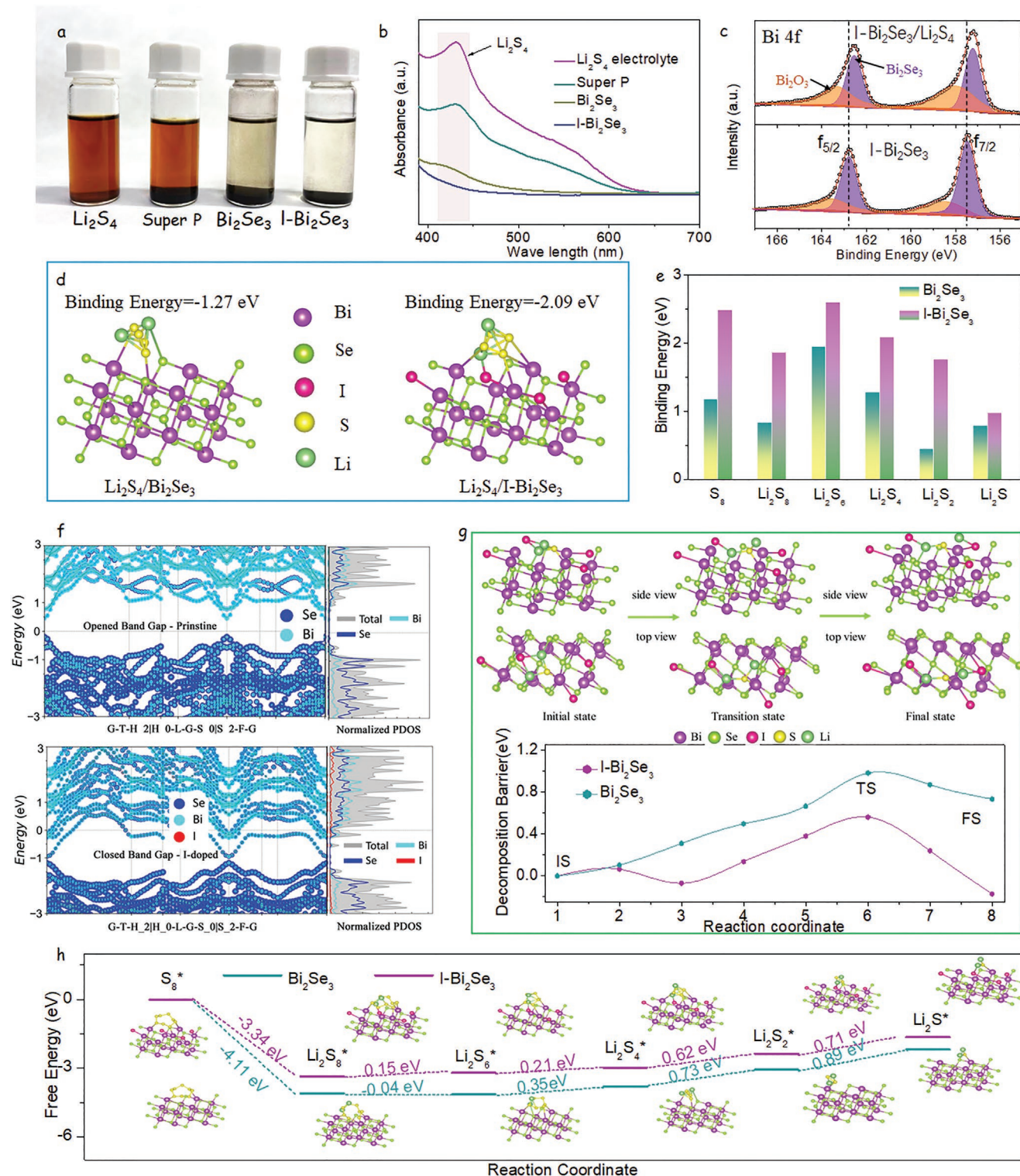
Figure 2. a) Optical photograph of flasks containing 3 mL of a 0.01 M Li_2S_4 solution and 20 mg of Super P, Bi_2Se_3, or I-Bi_2Se_3 after overnight aging. b) UV–vis spectra of the supernatants. c) Bi 4f XPS spectra of I-Bi_2Se_3 before and after Li_2S_4 adsorption. d) Optimized geometrical configurations of Li_2S_4 on Bi_2Se_3 and I-Bi_2Se_3 surfaces. e) Calculated binding energies of LiPS (Li_2S, Li_2S_2, Li_2S_4, Li_2S_6, Li_2S_8, and S_8) on Bi_2Se_3 and I-Bi_2Se_3 surfaces. f) HSE06 band structure and density of states of Bi_2Se_3 and I-Bi_2Se_3. g) Optimized adsorption configuration for the Li_2S decomposition on I-Bi_2Se_3 and energy barrier profiles of Li_2S cluster decomposition on Bi_2Se_3 and I-Bi_2Se_3 along with different reaction coordinates. h) Gibbs free energy profiles and optimized adsorption conformation of LiPS species on Bi_2Se_3 and I-Bi_2Se_3, showing a much lower reaction free energy from Li_2S_2 to Li_2S on I-Bi_2Se_3 than on Bi_2Se_3.
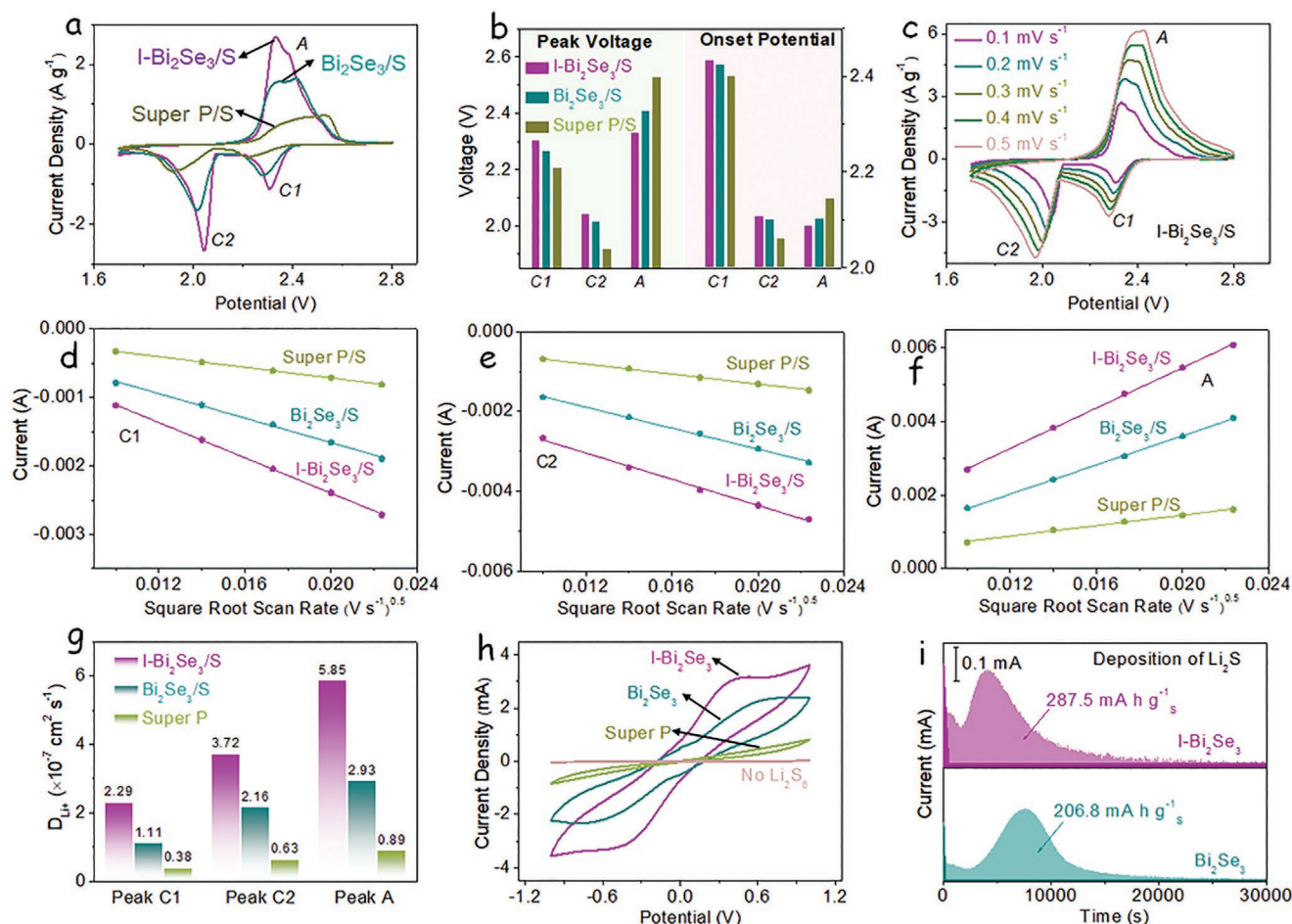
Figure 3. a) CV profiles of Li−S cells with I-Bi$_2$Se$_3$/S, Bi$_2$Se$_3$/S, and Super/S cathodes at a 0.1 mV s^{-1} scan rate. b) Peak potential and onset potential of asymmetrical Li−S cells obtained from CV curves. c) CV profiles of the I-Bi$_2$Se$_3$/S electrode at scan rates from 0.1 to 0.5 mV s^{-1}. d–f) Peak current versus the square root of the scan rate (v) for the cathodic reduction processes (C1, C2) and anodic oxidation process (A) in Li−S cells with different electrodes. g) Li$^+$ diffusion coefficient calculated from the CV redox peaks according to the Randles–Sevcik equation. h) CV curves of symmetric cells at a scan rate of 20 mV s^{-1}. i) Potentiostatic discharge profile at 2.05 V on different electrodes with Li$_2$S$_8$ catholyte for evaluating the nucleation kinetics of Li$_2$S.

The onset potentials at a current density of 10 µA cm^{-2} beyond the baseline current were used to quantitatively estimate the electrocatalytic activity (Figure 3b and Figure S10, Supporting Information).[23] Cells based on I-Bi$_2$Se$_3$/S cathodes showed the highest onset potentials of cathodic peaks and the lowest onset potentials for the anodic peak, which further demonstrates the accelerated redox kinetics obtained with the I-doped Bi$_2$Se$_3$ nanosheets. Figure S9, Supporting Information, displays the first five CV cycles measured from I-Bi$_2$Se$_3$/S cells. All CV curves almost overlapped, which suggests excellent reversibility of the sulfur redox reactions.

CV tests at different scan rates in the range 0.1–0.5 mV s^{-1} were conducted to investigate the reaction kinetics and the lithium-ion diffusion properties of I-Bi$_2$Se$_3$/S (Figure 3c). The peak current density of the I-Bi$_2$Se$_3$/S cathode increases with the scan rate, and its shape is maintained, which denotes good electrochemical stability. In contrast, Bi$_2$Se$_3$/S and especially Super P/S cathodes display more remarkable changes in the CV curve when increasing the scan rate, denoting limited reaction kinetics (Figure S11, Supporting Information).

I-Bi$_2$Se$_3$/S cathodes exhibited a linear relationship between the cathodic and anodic peak currents and the square root of the scanning rate, as it corresponds to a diffusion-limited process (Figure 3d–f). From the fitting of this linear dependence, the diffusion constant of the rate-limiting species, that is, lithium ions (D_{Li+}), was calculated according to the Randles-Sevcik equation:[5]

$$I_P = \left(2.69 * 10^5\right) n^{1.5} A D_{Li+}^{0.5} C_{Li+} v^{0.5} \tag{1}$$

where I_p is the peak current density, n is the number of charges transferred, A is the geometric area of the electrode, C_{Li+} is the concentration of lithium ions in the cathode, and v is the scan rate. I-Bi$_2$Se$_3$/S electrodes displayed the sharpest I_P versus $v^{0.5}$ slopes, indicating the fastest lithium-ion diffusion in both the reduction and oxidation processes. According to the Randles–Sevcik equation, the values of D_{Li+} calculated for I-Bi$_2$Se$_3$/S at peaks C1, C2, and A were 2.3×10^{-7}, 3.7×10^{-7}, and 5.9×10^{-7} cm^2 s^{-1}, respectively. All these values were well above those obtained for Bi$_2$Se$_3$/S and Super P/S electrodes

(Figure 3g). Taking into account the similar morphology of I-Bi$_2$Se$_3$ and Bi$_2$Se$_3$, the enhanced lithium-ion diffusivities must be related to the improved catalytic activity of the former, which accelerates the LiPS conversion, and to the stronger LiPS adsorption that suppresses the shuttle effect and prevents the deposition of an insulating layer at the anode side.[52]

To further analyze the electrocatalytic activity of the different materials toward the polysulfide conversion, CV profiles were measured on symmetric cells within the voltage window −1.0 to 1.0 V and using a 0.5 M Li$_2$S$_6$ electrolyte (Figure 3h).[5,34] To eliminate the capacitive contribution, the CV curve of I-Bi$_2$Se$_3$ in a Li$_2$S$_6$-free electrolyte was also measured as a reference (Figure S12, Supporting Information). The CV curve of the symmetric cells with a Li$_2$S$_6$-free electrolyte delivered a low current, well below that of CV curves of all symmetric cells having Li$_2$S$_6$ in their electrolyte, which indicates that the lithiation/delithiation reactions dominate the current response.[53] Besides, the I-Bi$_2$Se$_3$ symmetric cells including Li$_2$S$_6$ additive exhibited a much higher current density than those of Bi$_2$Se$_3$ and Super P cells, which we associate with an enhanced polysulfide absorption and a higher catalytic activity.

The Li$_2$S nucleation and dissolution processes were analyzed to investigate the liquid–solid reaction kinetics. Compared with the Bi$_2$Se$_3$ cathode, the I-Bi$_2$Se$_3$ cathode exhibited significantly shorter nucleation and growth times and a higher discharging peak current during the potentiostatic measurement at 2.05 V (Figure 3i). Based on Faraday´s law, the capacity of the I-Bi$_2$Se$_3$ electrode was calculated at 287.5 mAh g^{-1}, well above that of the Bi$_2$Se$_3$ electrode, 206.8 mAh g^{-1}.[54] Taking into account the similar morphology and crystal structure of the two materials, the significant differences obtained must be ascribed to the effect of iodine doping, which significantly improves the Li$_2$S precipitation kinetics.

The galvanostatic charge/discharge curves (GCDs) of I-Bi$_2$Se$_3$/S, Bi$_2$Se$_3$/S, and Super P/S electrodes at a current density of 0.1 C (1672 mA g^{-1}) are shown in **Figure 4**a. Charge/discharge curves display two discharge plateaus and one charge plateau, consistently with CV curves. The first discharge plateau at around 2.3 V is related to the reduction of sulfur to soluble LiPS (S$_8$ → S$_6^{2-}$ → S$_4^{2-}$).[55,56] The second discharge plateau corresponds to the conversion of soluble LiPS to lithium sulfide (S$_4$ → Li$_2$S$_2$ → Li$_2$S) at about 2.1 V.[57,58] The voltage difference between the oxidation and the second reduction plateaus is considered as

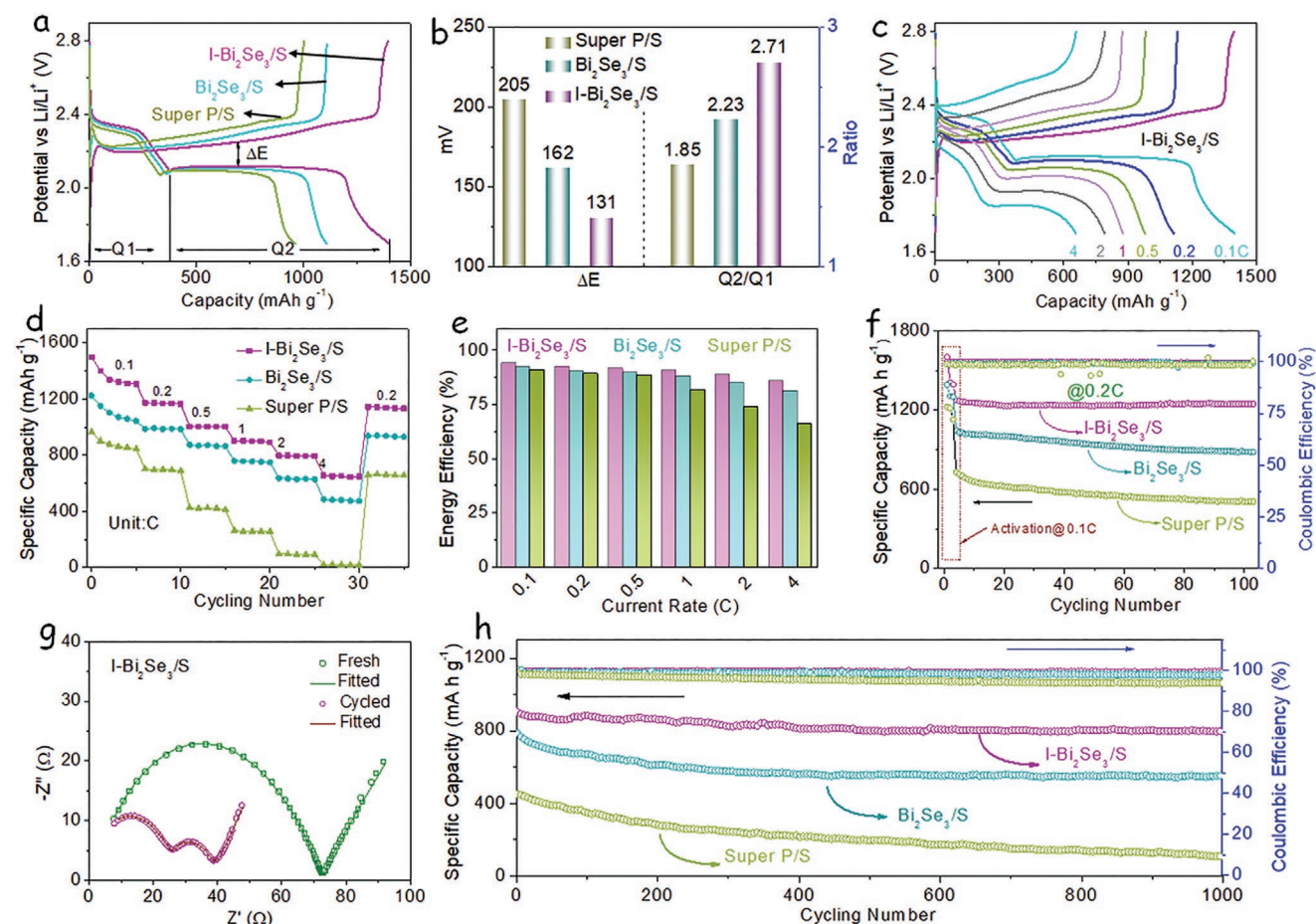**Figure 4.** a) GCD profiles of I-Bi$_2$Se$_3$/S, Bi$_2$Se$_3$/S, and Super/S electrodes at a 0.1 C current rate. b) ΔE and Q2/Q1 obtained from the charge/discharge curves. c) GCD profiles at various rates, from 0.1 to 4 C. d) Rate capability of different electrodes at various C rates, from 0.1 to 4 C. e) Energy efficiency of different cathodes at different current rates. f) Cycling performances of I-Bi$_2$Se$_3$/S, Bi$_2$Se$_3$/S, and Super/S electrodes at 0.2 C. g) EIS spectrum of the I-Bi$_2$Se$_3$/S electrode after and before cycling. h) Cycling performance and CE of the three cathodes at a current rate of 1 C.

ADVANCED
SCIENCE NEWS
www.advancedsciencenews.com

ADVANCED
FUNCTIONAL
MATERIALS
www.afm-journal.de

the polarization potential, ΔE.[59,60] Among the tested materials, I-Bi$_2$Se$_3$/S showed the lowest ΔE, at 131 mV, well below that of Bi$_2$Se$_3$/S, 162 mV, and Super P/S, 205 mV (Figure 4b).

Q1 and Q2 are defined as the capacity of the first and the second discharge plateaus, respectively. Q1 measures the amount of soluble polysulfides created and potentially diffusing to the Li metal anode. Q2 measures how efficiently the created polysulfides are reduced to Li$_2$S. Thus the ratio Q2/Q1 can be used as a measure of the catalytic activity for LiPS conversion reaction.[61] The Q2/Q1 ratio for I-Bi$_2$Se$_3$/S was 2.71, close to the theoretical limit of 3, and well above the values obtained from Bi$_2$Se$_3$/S and Super P/S, 2.23 and 1.85, respectively (Figure 4b). The high Q2/Q1 ratio of I-Bi$_2$Se$_3$/S implies a high catalytic activity toward polysulfide's redox reaction.

The charge and discharge profiles of the different electrodes displayed in Figure S13, Supporting Information, show the I-Bi$_2$Se$_3$/S electrode to be characterized by significantly lower overpotentials for phase conversion between soluble LiPS and insoluble Li$_2$S$_2$/Li$_2$S, which further demonstrates the enhanced electrochemical kinetics of I-Bi$_2$Se$_3$/S.[62]

The GCD voltage profiles of I-Bi$_2$Se$_3$/S electrodes at various current densities, from 1.0 to 4 C, are shown in Figure 4c. Two discharge plateaus and one charge plateau were maintained even at the highest current rates tested, which is in contrast with the results obtained from Super P/S electrodes (Figure S14, Supporting Information). An outstanding initial specific capacity of 1496 mAh g^{-1} was measured from the I-Bi$_2$Se$_3$/S electrode. Additionally, this electrode demonstrated a superior rate performance, with average discharge capacities of 1361, 1168, 1002, 897, 795, and 651 mAh g^{-1} at current rates from 0.1 to 4 C, respectively (Figure 4d). Even when the current density was returned to 0.2 C, the specific capacity of the I-Bi$_2$Se$_3$/S electrode was recovered to 1138 mAh g^{-1}, suggesting high stability even after the high rate charge/discharge process. All these values were clearly above those obtained from Bi$_2$Se$_3$/S and Super P/S electrodes.

Among the tested materials, the cells based on I-Bi$_2$Se$_3$/S were also characterized by the highest energy efficiencies (Figure 4e), as calculated from $E = \int UIdt$.[63] I-Bi$_2$Se$_3$/S based cells displayed an energy efficiency of 85.8% at 4 C, higher than Bi$_2$Se$_3$/S (80.9%) and Super P/S (66.1%) cells. The high energy efficiency measured for I-Bi$_2$Se$_3$/S was consistent with the lower polarization potential and higher catalytic properties of I-Bi$_2$Se$_3$.

Figure 4f shows the cycling performance of the different cathodes. In this test, the first three cycles were measured at a current density of 0.1 C, and then 100 cycles were tested at a current density of 0.2 C. The three electrodes showed a notably stable cycling performance during 100 cycles, with a coulombic efficiency (CE) above 99%. At 0.2 C, I-Bi$_2$Se$_3$/S electrodes displayed a high initial specific capacity (1274 mAh g^{-1}), well above that of Bi$_2$Se$_3$/S (1045 mAh g^{-1}), and Super P/S (727 mAh g^{-1}). After 100 cycles, 97.7% of the initial capacity was still retained for the I-Bi$_2$Se$_3$/S electrodes (1245 mAh g^{-1}). In contrast, the Bi$_2$Se$_3$/S cathode maintained just an 84.4% (882 mAh g^{-1}) of the initial discharge capacity, and the Super P/S cathode preserved just a 69.6% (506 mAh g^{-1}) of the initial capacity. The capacity loss in these cathodes was mainly associated with the dissolution of polysulfides into the electrolyte. Thus the high cycling stability of I-Bi$_2$Se$_3$/S was related to the effective inhibition of this dissolution.

Electrochemical impedance spectroscopy (EIS) was used to gain understanding of the parameters behind the enhanced redox kinetics of I-Bi$_2$Se$_3$/S electrodes. Figure 4g and Figure S15, Supporting Information, display the Nyquist plots of the EIS data obtained from I-Bi$_2$Se$_3$/S, Bi$_2$Se$_3$/S, and Super P/S coin cells before and after cycling. The fresh electrodes displayed a semicircle in the high-frequency region associated with the charge-transfer resistance (R_{ct}), followed by a linear dependence in the low-frequency region that is related to the diffusion of lithium ions.[64] After charge/discharge loops, an additional semicircle appeared in the high-frequency range, which is associated with the deposition of the insulating discharge products of Li$_2$S on the electrode surface (R_{in}) during cycling. Based on the equivalent circuit displayed in Figure S15, Supporting Information,[65] the I-Bi$_2$Se$_3$/S electrode has a considerably lower R_{in} and R_{ct} compared with Bi$_2$Se$_3$/S and Super P/S electrodes. These lower resistances indicate that the I-Bi$_2$Se$_3$/S electrode is characterized by a faster polysulfide conversion reaction, as well as a faster charge transfer kinetics during lithiation/delithiation reaction. Figure S16, Supporting Information, shows the XRD pattern of electrode materials after 100 cycles at 1 C, I-Bi$_2$Se$_3$ nanomaterials still maintained the rhombohedral phase with high crystallinity, which clearly indicated its high chemical stability during the charging and discharging processes of LSBs.

Even at a high current rate of 1C, I-Bi$_2$Se$_3$/S electrodes displayed a high specific capacity and stable cycling performance, with an average 0.012% capacity decay per cycle after 1000 cycles and CEs above 99.6%. The performance of I-Bi$_2$Se$_3$/S electrodes in this direction was also clearly above that of Bi$_2$Se$_3$/S and Super P/S (Figure 4h).

I-Bi$_2$Se$_3$ electrodes were further tested with a high sulfur loading (5.2 mg cm^{-2}) and a lean electrolyte (8 µL mg^{-1}) to demonstrate their potential application in practical LSBs. As shown in **Figure 5**a, high sulfur loading cells exhibited an excellent rate performance, with areal capacities of 5.70 mAh cm^{-2} at 0.1 C, and 4.12 mAh cm^{-2} at 0.5 C, that is, exceeding the industrially requested areal capacity of LIBs ($\approx$4 mAh cm^{-2}).[66] The corresponding charge/discharge profiles at different current rates are shown in Figure 5b. A small increase of voltage in the initial charges is probably related to an initial poor electrochemical contact between the electrolyte and the internal sulfur particles, which is a common observation at high sulfur loadings. With the current rate increasing to 0.5 C, the discharge profile still presented the intact second plateau, demonstrating excellent electrochemical kinetics within the cell. The performance of the cell under lean electrolyte conditions, with an electrolyte/sulfur ratio of 8 µL mg^{-1}, is displayed in Figure 5c. At a current rate of 0.5 C, the initial discharge capacity was 527 mAh g^{-1} and it rapidly increased to 686 mAh g^{-1} after 15 cycles. After 300 cycles, a capacity of 576 mAh g^{-1} was still measured, which corresponds to an ultralow capacity decay of 0.053% per cycle with respect to the maximum achieved capacity. Besides, I-Bi$_2$Se$_3$-based cells maintained the voltage profile during the 300 cycles, with just a small potential hysteresis, indicating a minor LiPS shuttling and stable sulfur electrochemistry (Figure S17, Supporting Information).

Figure 5d and Table S1, Supporting Information, display a comparison of several parameters of state-of-the-art Bi-based and Se-based materials as cathode hosts for LSBs. Notice that
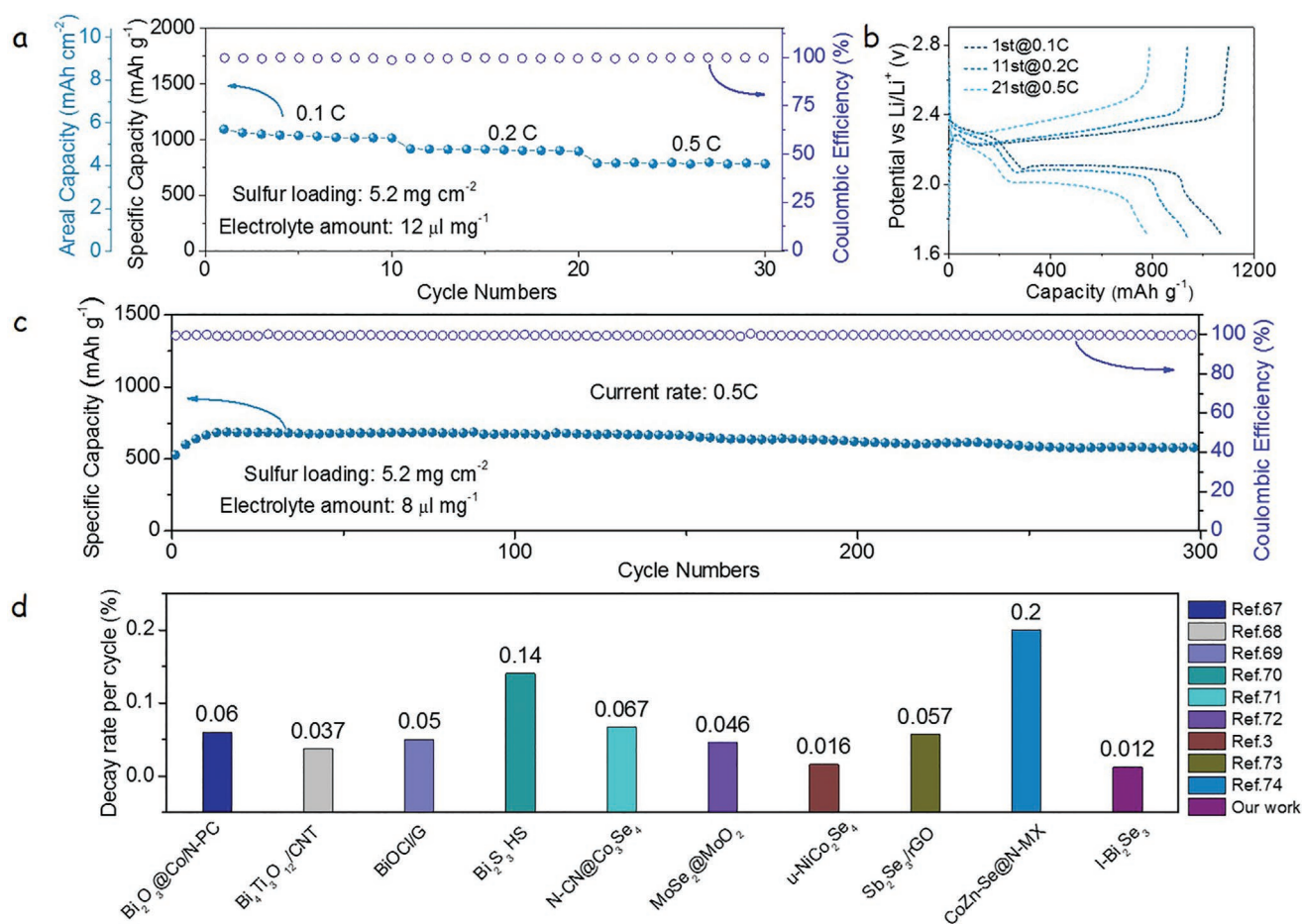
Figure 5. a) Rate performance of the Li—S coin cells at different current rates with a sulfur loading of 5.2 mg cm^{-2}. b) Initial charge/discharge profiles at the various current rates. c) Cycling performances of I-Bi$_2$Se$_3$/S cathodes at a current rate of 0.5 C under lean electrolyte conditions. d) Decay rate per cycle compared with other reported works.

the I-Bi$_2$Se$_3$ host presented here is characterized by the highest capacities and stabilities. This strategy offers a new route to design multifunctional sulfur immobilizer with highly adoptive and catalytic capabilities for rapid LiPS adsorption-conversion process, holding a great promise in promoting the practical application of LSBs.

Finally, a cycled I-Bi$_2$Se-based cell was disassembled and the composition of both the anode and the cathode was analyzed by EDX. We observed the anode to contain no iodine and just a small amount of sulfur (Figure S18, Supporting Information), which probed the I-Bi$_2$Se$_3$-based cathode to effectively inhibit the polysulfides "shuttle effect". EDX analysis of the cathode material after cycling showed the concentration of iodine to be maintained within the experimental error during the cycling (Figure S19, Supporting Information). The excellent iodine stability within the Bi$_2$Se$_3$ is related to the notable bond strength between Bi and I as calculated by DFT (Figure S20, Supporting Information).

3. Conclusion

In summary, we rationally designed and engineered new LSBs cathodes based on I-Bi$_2$Se$_3$ sulfur hosts through a facile and

efficient strategy. This unique architecture not only establishes a conductive framework for electron/ion transfer and buffers the volume variation of the sulfur cathode during cycling but also constructs a multifunctional LiPS barrier that effectively suppresses polysulfide shuttling. I-Bi$_2$Se$_3$ was characterized by a high electrical conductivity due to the doping of iodine and significantly enhanced the redox kinetics of sulfur species, especially for the conversion between soluble LiPS species and Li$_2$S$_2$/Li$_2$S during charge/discharge processes. As a result of these excellent qualities, I-Bi$_2$Se$_3$/S cathodes deliver excellent long-term cycling stability with a capacity decay of 0.012% per cycle over 1000 cycles at 1 C. Moreover, at a sulfur loading of 5.2 mg cm^{-2}, I-Bi$_2$Se$_3$/S cathodes delivered a high areal capacity of 5.70 mAh cm^{-2}. Overall, this work shows an effective way to enhance the performance of LSB cathodes by the heteroatom doping of a metal selenide catalyst.

4. Experimental Section

Chemicals: Bismuth(III) nitrate pentahydrate (Bi(NO$_3$)$_3$·5H$_2$O, ≥99.99%), sodium selenite (Na$_2$SeO$_3$, ≥98%), ethylene glycol (EG, HOCH$_2$CH$_2$OH, 99%), and potassium hydroxide (KOH, ≥98%) were

acquired from Fisher. Polyvinylpyrrolidone (PVP, $(C_6H_9NO)_n$, AMW ≈ 55 000), were purchased from Sigma Aldrich. Ethanol and acetone were obtained from various sources at analytical grade.

Synthesis of Bi_2Se_3: $Bi(NO_3)_3 \cdot 5H_2O$ (2 mmol), Na_2SeO_3 (3 mmol), KOH (10 mmol), and PVP (0.1 g) were dissolved in a three-neck flask containing EG (50 mL) under Ar atmosphere at ambient temperature for 0.5 h. The solution was then heated to 180 °C and kept at this temperature for 3 h. Immediately after the reaction was completed, the solution was allowed to cool naturally to room temperature by removing the heating mantle. The solution was divided into several centrifuge tubes and acetone was added to collect the solid product by centrifugation. In the next step, ethanol was introduced to re-disperse the particles and acetone to precipitate them again. This step was repeated twice. After that, purified Bi_2Se_3 particles were dried under vacuum overnight at room temperature.

Synthesis of I-Bi_2Se_3: 2.5 mg KI were dissolved in 5 mL deionized water. Then, 0.2 g dried Bi_2Se_3 nanosheets were added to the solution, kept in N_2-filled vials, and vigorously stirred at room temperature for 48 h. After that, ethanol was added to the mixture to precipitate the nanosheets by centrifugation. Subsequently, the nanosheets were washed one more time with ethanol, centrifuged, and dried under vacuum.

Synthesis of I-Bi_2Se_3/S, Bi_2Se_3/S, and Super P/S: Sulfur was added through a simple melting infiltration process. I-Bi_2Se_3/S was obtained by mixing I-Bi_2Se_3 nanosheets and sublimed sulfur in a weight ratio of 1:3 and heated at 155 °C for 12 h in a glass bottle under an Ar atmosphere. After that, the powder was immersed in a 10 mL CS_2 and ethanol solution (1:4 volume ratio) for 10 min twice. For comparison, Bi_2Se_3/S and Super P/S were obtained by the same process.

Materials Characterization: An Auriga Zeiss field emission scanning electron microscope (SEM) was used to determine the nanoparticle morphology. An Oxford EDX was used to measure the material composition at 20.0 kV. XRD was performed on a Bruker AXS D8 Advance diffractometer. XPS was performed on a Specs system with the material inside the chamber at a pressure below 10^{-7} Pa. Data processing was carried out using the CasaXPS program. Crystallographic structure and chemical composition were analyzed by HRTEM and EELS, respectively, using a Tecnai F20 field-emission gun microscope at 200 kV with an embedded Gatan Quantum image filter. TGA was performed to record the ratio of S within prepared composites (PerkinElmer Diamond TG/DTA instrument). A Perkin Elmer Lambda 950 UV–vis spectrophotometer was used to measure UV–vis absorption spectra. Nitrogen adsorption–desorption isotherms were measured on a Tristar II 3020 Micromeritics system to evaluate the specific surface area and the pore size distribution using a BET method.

Electrochemical Measurements: Cathodes were prepared by mixing the active materials (I-Bi_2Se_3/S, Bi_2Se_3/S, and Super P/S), Super P, and PVDF binders in a weight ratio of 8:1:1 in N-methyl-2-pyrrolidone. The slurry was applied on aluminum foil and dries under vacuum at 60 °C overnight. Subsequently, the coated aluminum foil was punched into small disks (12.0 mm) with a sulfur content of about 1 mg cm^{-2}, and assembled into a coin unit in a glove box filled with Ar. Li foil was used as the counter electrode and Celgard 2400 membranes as separators. The electrolyte was prepared by dissolving 1.0 M lithium bis(trifluoromethanesulfonyl)imide and 0.2 M $LiNO_3$ in a mixture of DOL and DME with a volume ratio of 1:1. The amount of electrolyte was about 20 µL for each coin cell. For the higher sulfur loading electrodes, 3.2 mg cm^{-2}, 50 µL of electrolyte was added to the coin cell. Before cycling, all coin cells undergo aging for several hours to ensure that the electrolyte fully penetrates the electrodes. GCD measurements were performed with a voltage window of 1.7–2.8 V versus Li$^+$/Li at different current densities using a Neware BTS4008 battery cycler. Cyclic voltammetry (CV) tests were performed on a BCS-810 battery tester from BioLogic at different scan rates in the range of 0.1–0.5 mV s^{-1}. Sinusoidal voltage with an amplitude of 10 mV in the frequency range 100 kHz to 0.01 Hz was used to measure EIS.

Synthesis of Li_2S_4 Solution and Adsorption Test: Sulfur and Li_2S with a molar ratio of 3:1 were dissolved in the DME and DOL solution (volume ratio of 1:1), then vigorous magnetic stirring overnight and turned to a dark brown solution. For the polysulfide absorption ability test, 20 mg of I-Bi_2Se_3, Bi_2Se_3, and Super P was immersed into a 3.0 mL mixture solution above, respectively, shaken and aged overnight.

Symmetric Cell Assembly and Measurements: Electrodes (I-Bi_2Se_3, Bi_2Se_3, and Super P) for symmetric cells were fabricated in the same way as electrodes for LSBs. Two pieces of the same electrode (average loading about 0.5 mg cm^{-2}) were used as identical working and counter electrodes. A 40 µL amount of electrolyte containing 0.5 M Li_2S_6 and 1 M LiTFSI dissolved in DOL/DME (v/v = 1:1) was added into each coin cell. CV measurements were performed at scan rate of 10 mV s^{-1}, and EIS tests were carried out in the frequency range 100 kHz to 0.01 Hz.

Measurement of Nucleation of Li_2S: Nucleation of Li_2S was studied in standard 2032 coin cells. Dispersing the same amount of I-Bi_2Se_3 Bi_2Se_3 and Super P composites in ethanol, and then coat them in carbon paper as the cathode. Li foil was used as the counter electrode. A 20 µL amount of 0.25 M Li_2S_8 with 1.0 M LiTFSI in tetraethylene glycol dimethyl ether solution was used as catholyte, and 20 µL of a 1.0 M LiTFSI solution without Li_2S_8 was used as anolyte. Coin cells were held at 2.06 V to reduce the generation of higher-order LiPS than Li_2S_4. Then the cells were potentiostatically discharged at 2.05 V until the current decreased to 10^{-5} A.

Supporting Information

Supporting Information is available from the Wiley Online Library or from the author.

Conflict of Interest

The authors declare no conflict of interest.

Data Availability Statement

The data that support the findings of this study are available from the corresponding author upon reasonable request.

[1] J. Zheng, J. Tian, D. Wu, M. Gu, W. Xu, C. Wang, F. Gao, M. H. Engelhard, J. G. Zhang, J. Liu, J. Xiao, *Nano Lett.* **2014**, *14*, 2345.

[2] Z. Wang, B. Wang, Y. Yang, Y. Cui, Z. Wang, B. Chen, G. Qian, *ACS Appl. Mater. Interfaces* **2015**, *7*, 20999.

[3] C. Zhang, J. J. Biendicho, T. Zhang, R. Du, J. Li, X. Yang, J. Arbiol, Y. Zhou, J. R. Morante, A. Cabot, *Adv. Funct. Mater.* **2019**, *29*, 1903842.

[4] Y. Song, Y. Peng, M. Zhao, Y. Lu, J. Liu, B. Li, Q. Zhang, *Small Sci.* **2021**, *1*, 2100042.

[5] D. Yang, Z. Liang, C. Zhang, J. J. Biendicho, M. Botifoll, M. C. Spadaro, Q. Chen, M. Li, A. Ramon, A. O. Moghaddam, J. Llorca, J. Wang, J. R. Morante, J. Arbiol, S. L. Chou, A. Cabot, *Adv. Energy Mater.* **2021**, *11*, 2101250.

[6] S. Bai, X. Liu, K. Zhu, S. Wu, H. Zhou, *Nat. Energy* **2016**, *1*, 16049.

[7] C. Zhao, X. Dai, T. Yao, W. Chen, X. Wang, J. Wang, J. Yang, S. Wei, Y. Wu, Y. Li, *J. Am. Chem. Soc.* **2017**, *139*, 8078.

[8] C. Zheng, S. Niu, W. Lv, G. Zhou, J. Li, S. Fan, Y. Deng, Z. Pan, B. Li, F. Kang, Q. H. Yang, *Nano Energy* **2017**, *33*, 306.

[9] S. Tu, X. Chen, X. Zhao, M. Cheng, P. Xiong, Y. He, Q. Zhang, Y. Xu, *Adv. Mater.* **2018**, *30*, 1804581.

[10] H. Jiang, X.-C. Liu, Y. Wu, Y. Shu, X. Gong, F.-S. Ke, H. Deng, *Angew. Chem.* **2018**, *130*, 3980.

[11] M. Tian, F. Pei, M. Yao, Z. Fu, L. Lin, G. Wu, G. Xu, H. Kitagawa, X. Fang, *Energy Storage Mater.* **2019**, *21*, 14.

[12] X. J. Hong, C. L. Song, Y. Yang, H. C. Tan, G. H. Li, Y. P. Cai, H. Wang, *ACS Nano* **2019**, *13*, 1923.

[13] D. Yang, Z. Liang, P. Tang, C. Zhang, M. Tang, Q. Li, J. J. Biendicho, J. Li, M. Heggen, R. E. Dunin-Borkowski, M. Xu, J. Llorca, J. Arbiol, J. R. Morante, S. L. Chou, A. Cabot, *Adv. Mater.* **2022**, *34*, 2108835.

[14] J. Shen, X. Xu, J. Liu, Z. Liu, F. Li, R. Hu, J. Liu, X. Hou, Y. Feng, Y. Yu, M. Zhu, *ACS Nano* **2019**, *13*, 8986.

[15] B. Jin, L. Yang, J. Zhang, Y. Cai, J. Zhu, J. Lu, Y. Hou, Q. He, H. Xing, X. Zhan, F. Chen, Q. Zhang, *Adv. Energy Mater.* **2019**, *9*, 1902938.

[16] Z. Li, Z. Xiao, S. Wang, Z. Cheng, P. Li, R. Wang, *Adv. Funct. Mater.* **2019**, *29*, 1902322.

[17] J. Xie, B. Q. Li, H. J. Peng, Y. W. Song, M. Zhao, X. Chen, Q. Zhang, J. Q. Huang, *Adv. Mater.* **2019**, *31*, 1903813.

[18] L. Zhang, D. Liu, Z. Muhammad, F. Wan, W. Xie, Y. Wang, L. Song, Z. Niu, J. Chen, *Adv. Mater.* **2019**, *31*, 1903955.

[19] H. Chen, Y. Xiao, C. Chen, J. Yang, C. Gao, Y. Chen, J. Wu, Y. Shen, W. Zhang, S. Li, F. Huo, B. Zheng, *ACS Appl. Mater. Interfaces* **2019**, *11*, 11459.

[20] Y. He, Y. Qiao, Z. Chang, X. Cao, M. Jia, P. He, H. Zhou, *Angew. Chem.* **2019**, *131*, 11900.

[21] B. Li, L. Kong, C. Zhao, Q. Jin, X. Chen, H. Peng, J. Qin, J. Chen, H. Yuan, Q. Zhang, J. Huang, *InfoMat* **2019**, *1*, 533.

[22] Y. Zheng, S. Zheng, H. Xue, H. Pang, *J. Mater. Chem. A* **2019**, *7*, 3469.

[23] H. Chu, H. Noh, Y. J. Kim, S. Yuk, J. H. Lee, J. Lee, H. Kwack, Y. K. Kim, D. K. Yang, H. T. Kim, *Nat. Commun.* **2019**, *10*, 188.

[24] S. Zhou, S. Yang, S. Yang, X. Ding, Y. Lai, H. Nie, Y. Zhang, D. Chan, H. Duan, S. Huang, Z. Yang, *ACS Nano* **2020**, *14*, 7538.

[25] L. Luo, J. Li, H. Yaghoobnejad Asl, A. Manthiram, *ACS Energy Lett.* **2020**, *5*, 1177.

[26] Z. Sun, S. Vijay, H. H. Heenen, A. Y. S. Eng, W. Tu, Y. Zhao, S. W. Koh, P. Gao, Z. W. Seh, K. Chan, H. Li, *Adv. Energy Mater.* **2020**, *10*, 201904010.

[27] Z. Cheng, Y. Wang, W. Zhang, M. Xu, *ACS Appl. Energy Mater.* **2020**, *3*, 4523.

[28] G. Li, F. Lu, X. Dou, X. Wang, D. Luo, H. Sun, A. Yu, Z. Chen, *J. Am. Chem. Soc.* **2020**, *142*, 3583.

[29] W. Liu, C. Luo, S. Zhang, B. Zhang, J. Ma, X. Wang, W. Liu, Z. Li, Q. H. Yang, W. Lv, *ACS Nano* **2021**, *15*, 7491.

[30] W. Hua, H. Li, C. Pei, J. Xia, Y. Sun, C. Zhang, W. Lv, Y. Tao, Y. Jiao, B. Zhang, S. Z. Qiao, Y. Wan, Q. H. Yang, *Adv. Mater.* **2021**, *33*, 2101006.

[31] T. Feng, T. Zhao, S. Zhu, N. Zhang, Z. Wei, K. Wang, L. Li, F. Wu, R. Chen, *Small Methods* **2021**, *5*, 2100649.

[32] Z. Ma, Y. Liu, J. Gautam, W. Liu, A. N. Chishti, J. Gu, G. Yang, Z. Wu, J. Xie, M. Chen, L. Ni, G. Diao, *Small* **2021**, *17*, 2102710.

[33] X. Zhou, R. Meng, N. Zhong, S. Yin, G. Ma, X. Liang, *Small Methods* **2021**, *5*, 2100571.

[34] D. Yang, C. Zhang, J. J. Biendicho, X. Han, Z. Liang, R. Du, M. Li, J. Li, J. Arbiol, J. Llorca, Y. Zhou, J. R. Morante, A. Cabot, *ACS Nano* **2020**, *14*, 15492.

[35] Y. Zhang, S. Yang, S. Zhou, L. Zhang, B. Gu, Y. Dong, S. Kong, D. Cai, G. Fang, H. Nie, Z. Yang, *Chem. Commun.* **2021**, *57*, 3255.

[36] Y. Zhang, J. Liu, J. Wang, Y. Zhao, D. Luo, A. Yu, X. Wang, Z. Chen, *Angew. Chem.* **2021**, *60*, 202108882.

[37] Y. Li, S. Lin, D. Wang, T. Gao, J. Song, P. Zhou, Z. Xu, Z. Yang, N. Xiao, S. Guo, *Adv. Mater.* **2020**, *32*, 1906722.

[38] S. Li, J. Lin, Y. Ding, P. Xu, X. Guo, W. Xiong, D.-Y. Wu, Q. Dong, J. Chen, L. Zhang, *ACS Nano* **2021**, *15*, 13803.

[39] T. Zhang, F. Hu, W. Shao, S. Liu, H. Peng, Z. Song, C. Song, N. Li, X. Jian, *ACS Nano* **2021**, *15*, 15027.

[40] H. Lin, H. Shi, Z. Wang, Y. Mu, S. Li, J. Zhao, J. Guo, B. Yang, Z. Wu, F. Liu, *ACS Nano* **2021**, *15*, 17327.

[41] T. Yang, J. Xia, Z. Piao, L. Yang, S. Zhang, Y. Xing, G. Zhou, *ACS Nano* **2021**, *15*, 13901.

[42] C. Zhang, R. Du, J. J. Biendicho, M. Yi, K. Xiao, D. Yang, T. Zhang, X. Wang, J. Arbiol, J. Llorca, Y. Zhou, J. R. Morante, A. Cabot, *Adv. Energy Mater.* **2021**, *11*, 2100432.

[43] H. Yuan, H. J. Peng, B. Q. Li, J. Xie, L. Kong, M. Zhao, X. Chen, J. Q. Huang, Q. Zhang, *Adv. Energy Mater.* **2019**, *9*, 1802768.

[44] G. E. Lee, I. H. Kim, Y. S. Lim, W. S. Seo, B. J. Choi, C. W. Hwang, *J. Korean Phys. Soc.* **2014**, *65*, 696.

[45] M. Li, Y. Zhang, T. Zhang, Y. Zuo, K. Xiao, J. Arbiol, J. Llorca, Y. Liu, A. Cabot, *Nanomaterials* **2021**, *11*, 1827.

[46] M. Hong, Z. G. Chen, L. Yang, G. Han, J. Zou, *Adv. Electron. Mater.* **2015**, *1*, 1500025.

[47] P. H. Le, K. H. Wu, C. W. Luo, J. Leu, *Thin Solid Films* **2013**, *534*, 659.

[48] A. J. Green, S. Dey, Y. Q. An, B. O'Brien, S. O'Mullane, B. Thiel, A. C. Diebold, *J. Vac. Sci. Technol., A* **2016**, *34*, 061403.

[49] T. Li, Y. Hu, C. A. Morrison, W. Wu, H. Han, N. Robertson, *Sustainable Energy Fuels* **2017**, *1*, 308.

[50] J. Betancourt, S. Li, X. Dang, J. D. Burton, E. Y. Tsymbal, J. P. Velev, *J. Phys.: Condens. Matter* **2016**, *28*, 395501.

[51] Z. Li, P. Li, X. Meng, Z. Lin, R. Wang, *Adv. Mater.* **2021**, *33*, 2102338.

[52] S. Kim, W.-G. Lim, H. Im, M. Ban, J. W. Han, J. Lee, J. Hwang, J. Lee, *J. Am. Chem. Soc.* **2021**, *143*, 15644.

[53] H. Zhang, L. K. Ono, G. Tong, Y. Liu, Y. Qi, *Nat. Commun.* **2021**, *12*, 4738.

[54] W. Xiao, W. Weng, J. Xiao, Y. Shen, X. Liang, T. Lv, *Angew. Chem.* **2021**, *60*, 202111707.

[55] J. Kim, H. Shin, D. J. Yoo, S. Kang, S. Y. Chung, K. Char, J. W. Choi, *Adv. Funct. Mater.* **2021**, *31*, 2106679.

[56] G. Zhou, G. Zhou, A. Yang, G. Gao, X. Yu, J. Xu, C. Liu, Y. Ye, A. Pei, Y. Wu, Y. Peng, Y. Li, Z. Liang, K. Liu, L. W. Wang, Y. Cui, Y. Cui, *Sci. Adv.* **2020**, *6*, eaay5098.

[57] J. Liu, H. Li, J. Wang, Y. Zhang, D. Luo, Y. Zhao, Y. Li, A. Yu, X. Wang, Z. Chen, *Adv. Energy Mater.* **2021**, *11*, 2101926.

[58] Z. Han, S. Zhao, J. Xiao, X. Zhong, J. Sheng, W. Lv, Q. Zhang, G. Zhou, H. M. Cheng, *Adv. Mater.* **2021**, *33*, 2105947.

[59] Y. Ji, K. Yang, M. Liu, S. Chen, X. Liu, B. Yang, Z. Wang, W. Huang, Z. Song, S. Xue, Y. Fu, L. Yang, T. S. Miller, F. Pan, *Adv. Funct. Mater.* **2021**, *31*, 2104830.

[60] R. Gao, Q. Zhang, Y. Zhao, Z. Han, C. Sun, J. Sheng, X. Zhong, B. Chen, C. Li, S. Ni, Z. Piao, B. Li, G. Zhou, *Adv. Funct. Mater.* **2021**, 2110313.

**ADVANCED
SCIENCE NEWS**

www.advancedsciencenews.com

**ADVANCED
FUNCTIONAL
MATERIALS**

www.afm-journal.de

[61] D. Cai, J. Yang, T. Liu, S. Zhao, G. Cao, *Nano Energy* **2021**, *89*, 106452.

[62] Y. Huang, M. Shaibani, T. D. Gamot, M. Wang, P. Jovanović, M. C. Dilusha Cooray, M. S. Mirshekarloo, R. J. Mulder, N. V. Medhekar, M. R. Hill, M. Majumder, *Nat. Commun.* **2021**, *12*, 5375.

[63] S. Chen, Z. Song, Y. Ji, K. Yang, J. Fang, L. Wang, Z. Wang, Y. Zhao, Y. Zhao, L. Yang, F. Pan, *Small Methods* **2021**, *5*, 2100839.

[64] H. Kang, M. J. Park, *Nano Energy* **2021**, *89*, 106459.

[65] D. Wang, K. Ma, J. Hao, W. Zhang, C. Wang, C. Xu, H. Shi, Z. Ji, X. Yan, Y. Gu, *Nano Energy* **2021**, *89*, 106426.

[66] C. Shang, G. Li, B. Wei, J. Wang, R. Gao, Y. Tian, Q. Chen, Y. Zhang, L. Shui, G. Zhou, Y. Hu, Z. Chen, X. Wang, *Adv. Energy Mater.* **2021**, *11*, 2003020.

[67] H. Liu, Z. Chen, L. Zhou, X. Li, K. Pei, J. Zhang, Y. Song, F. Fang, R. Che, D. Sun, *J. Mater. Chem. A* **2019**, *7*, 7074.

[68] Y. Zhou, H. Shu, Y. Zhou, T. Sun, M. Han, Y. Chen, M. Chen, Z. Chen, X. Yang, X. Wang, *J. Power Sources* **2020**, *453*, 227896.

[69] X. Wu, N. Liu, M. Wang, Y. Qiu, B. Guan, D. Tian, Z. Guo, L. Fan, N. Zhang, *ACS Nano* **2019**, *13*, 13109.

[70] B. Long, Z. Qiao, J. Zhang, S. Zhang, M. S. Balogun, J. Lu, S. Song, Y. Tong, *J. Mater. Chem. A* **2019**, *7*, 11370.

[71] D. Cai, B. Liu, D. Zhu, D. Chen, M. Lu, J. Cao, Y. Wang, W. Huang, Y. Shao, H. Tu, W. Han, *Adv. Energy Mater.* **2020**, *10*, 1904273.

[72] Q. Hao, G. Cui, Y. Zhang, J. Li, Z. Zhang, *Chem. Eng. J.* **2020**, *381*, 122672.

[73] Y. Tian, G. Li, Y. Zhang, D. Luo, X. Wang, Y. Zhao, H. Liu, P. Ji, X. Du, J. Li, Z. Chen, *Adv. Mater.* **2020**, *32*, 1904876.

[74] Z. Ye, Y. Jiang, L. Li, F. Wu, R. Chen, *Adv. Mater.* **2021**, *33*, 2101204.